Electronic Supplementary Information (ESI)

Engineering Transition Metal Hydroxide-Photoanode Interface with a Highly Crystalline Mediator for Efficient Photoelectrochemical Water Splitting

Meihua Li[1], Saqib Mujtaba[1], Li Xu, Chenglong Li, Jingjing Quan, Xingming Ning*, Pei Chen*, Qiang Weng, Zhongwei An, Xinbing Chen*

Key Laboratory of Applied Surface and Colloid Chemistry (MOE), Shaanxi Key Laboratory for Advanced Energy Devices, Shaanxi Engineering Laboratory for Advanced Energy Technology, International Joint Research Center of Shaanxi Province for Photoelectric Materials Science. School of Materials Science and Engineering, Shaanxi Normal University, Xi'an, 710119, PR China.

**Corresponding author, E-mail: ningxingming@snnu.edu.cn, chenpei@snnu.edu.cn, chenxinbing@snnu.edu.cn*

TABLE OF CONTENTS

S 1. Experimental Section

S 1.1 Materials and Reagents

Bismuth nitrate pentahydrate ($Bi(NO_3)_3 \cdot 5H_2O$, 98.00%) was selected from Alfa Aesar (China) Chemicals Co. Ltd. Potassium iodide (KI, ≥ 99.00%), Potassium ferrocyanide trihydrate ($K_4[Fe(CN)_6]$, ≥ 99.00%), Potassium ferricyanide ($K_3[Fe(CN)_6]$, ≥ 99.50%), Boric acid (H3BO3, 99.00%), Iron sulfate heptahydrate ($FeSO_4 \cdot 7H_2O$, ≥ 99.00%), Dimethyl sulfoxide (DMSO, > 99.00%), Vanadyl acetylacetonate ($VO(acac)_2$, 98.00%), and Cobalt nitrate hexahydrate ($Co(NO_3)_2 \cdot 6H_2O$, 99.00%) were obtained from Shanghai Aladdin Biochemical Technology Co., Ltd. Sodium sulfite (Na_2SO_3, ≥ 97.00%), p-Benzoquinone ($C_6H_4O_2$, ≥ 98.00%), Nickel(II) nitrate hexahydrate ($Ni(NO_3)_2 \cdot 6H_2O$, ≥ 98.00%), Potassium hydroxide (KOH, AR), Potassium chloride (KCl, ≥ 99.50%), Nitric acid (HNO_3, AR), Ethanol absolute (C_2H_6O, ≥ 99.70%), and Acetone (C_3H_6O, ≥ 99.50%) were obtained from Sinopharm Chemical Reagent Co., Ltd. Second water (18.2 MΩ cm) was used by a Milli-Q system (Milli-Q, Millipore Corp.). FTO substrates (F: SnO_2, 14 Ω per square) were ultrasonically cleaned for 15 min each in deionized water, ethanol and acetone, respectively.

S 1.2 Physical Measurements and Instruments

The morphology of different photoelectrodes was explored by field emission scanning electron microscopy (FESEM, SU8020). Transmission electron microscopy (TEM) and high-resolution TEM (HR-TEM) images were carried out using a Tecnai G^2 F30 (200 KV) with elements mapping. The chemical state and composition of samples were identified by X-ray photoelectron spectroscopy (XPS, Escalab Xi^+). The crystalline structures were obtained from X-ray diffraction analysis (XRD, Smart Lab 9 KW). Raman spectroscopy was measured by Microscopic confocal laser Raman spectrometer. UV/Vis diffuse reflectance spectroscopy (DRS) from 400 to 700 nm were taken on a UV-3600 (Shimadzu) spectrometer. Photoluminescence (PL) spectra (excitation of 350 nm) were tested on FL 8500 fluorescence spectrophotometer. Time-resolved photoluminescence (TRPL) spectroscopy was performed on Fluorolog-QM (HORIBA).

S 1.3 Electrochemical Measurements

Electrochemical tests were performed on CHI760E using a traditional three-electrode system, including FTO with different samples as working electrode. Cyclic

voltammogram (CV) curves were obtained with different scan rates for relevant samples, such as 200 mV/s, 100 mV/s and 50 mV/s.

S 1.4 Photoelectrochemical Measurements

The photoelectrochemical (PEC) activity of all samples were measured using 0.5 M phosphate-buffered saline (PBS) solution as the electrolyte, and BV-based photoanodes as working electrode (WE). The light source (300 W Xenon arc lamp, Beijing Perfectlight Technology Co. Ltd., PLS-SXE300D), equipped with an AM 1.5 G filter, was regarded as a simulated solar illumination AM 1.5 G (100 mW/cm^2). In the work, all illuminated areas of WE were 1 cm^2 (1 cm × 1 cm). The potential was adjusted to the RHE scale by the Nernst equation:[1]

$$E_{RHE} = E_{Ag/AgCl} + 0.197 + 0.0591\ pH$$

Photocurrent-potential curves were obtained with a scan rate of 50 mV/s, and current-time (*I-t*) curve of different photoanodes was operated at 1.0 V_{RHE} under AM 1.5 G. The following PEC properties were measured by Autolab M204. The electrochemical impedance spectroscopy (EIS) was measured at -0.2 V versus Ag/AgCl in the frequency range from 10 KHz to 0.1 Hz in 0.5 M PBS. The equivalent randles circuit consists of a series resistance (R_s), a charge transfer resistance (R_{ct}), and a constant phase element (CPE). According to our previous work, the intensity modulated photocurrent spectroscopy (IMPS) characterizations were conducted through photoEchem system (LED, 470 nm, 20% light intensity modulation) of Autolab M204. The IMPS plots were measured over a frequency range from 10 KHz to 0.1 Hz in 0.5 M PBS. And the *I-t* curves were carried out at the same potential with IMPS by using a light source (LED, 470 nm). The average lifetime (τ) can be achieved by the following formula:[2]

$$\tau_d = \frac{1}{2\pi f_{IMPS}}$$

Where f_{IMPS} is the frequency located of the lowest point in the IMPS plot.

The applied bias photon-to-current efficiency (ABPE) is calculated by the following equation:[3]

$$\mathrm{ABPE}(\%) = \frac{J \times \left(1.23 - V_b\right)}{P_{light}} \times 100\#$$

where J represents the photocurrent density (mA/cm^2), V_b represents the applied bias voltage (vs. RHE), and Plight is the intensity of AM 1.5 G (100 mW/cm^2).

The surface charge separation sufficiency (η_{sep}) can be calculated using the equation:[4]

$$\eta_{sep}(\%) = \frac{J_{H_2O}}{J_{Na_2SO_3}} \times 100\%$$

Where J_{H_2O} and $J_{Na_2SO_3}$ is the photocurrent density obtained in a 0.5 M phosphate-buffered saline (PBS) electrolyte without or with Na_2SO_3, respectively.

S 1.5 In situ Ultraviolet/visible-spectroelectrochemistry (in situ UV/vis-SEC) measurements

In situ Ultraviolet/visible-spectroelectrochemistry (UV/vis-SEC) measurements were performed by our home-built equipment. Herein, the substrate electrodes modified with different samples (BV, BV/FeNi$(OH)_X$ and BV/Fe$(OH)_X$-H/FeNi$(OH)_X$) were regarded as working electrode (WE). Meanwhile, platinum wire and Ag/AgCl were treated as auxiliary electrode and reference electrode, respectively. In addition, a soft probe molecule (i.e., $K_4[Fe(CN)_6]$) was employed as electrolyte. The potential of WE was selected 0.47 V vs Ag/AgCl during all tests. Under AM 1.5 G light irradiation, for different samples, BV will generate electrons and holes. These photogenerated electrons will directly transfer to FTO substrate, and these holes will transport from the valance band (VB) of BV to the surface of integrated photoanode. Owing to the redox potential of $[Fe(CN)_6]^{3-}/[Fe(CN)_6]^{4-}$ is 0.36 V_{RHE}, therefore, these accumulated holes are easily to oxidize $K_4[Fe(CN)_6]$ to $K_3[Fe(CN)_6]$, resulting in concentration changes of electrolyte in different systems. The different of concentration during oxidation reaction could be observed with UV/vis-SEC by monitoring new peaks and changes in the intensity or position from absorbance maximum. Where absorbance can be closely related to the concentration according to the Beer-Lambert Law.

S 2. Preparation Details

Preparation of nanoporous BV： The nanoporous BV photoanodes were synthesized by following the previously established methods of researchers. To initiate the process, 40 mmol KI was dissolved in 50 mL of second water, and the pH was adjusted to 1.7 by the addition of HNO_3. Then, 0.97 g of $Bi(NO_3)_3 \cdot 5H_2O$ was gradually introduced into the solution, which was then mixed with 20 mL of 100% ethanol containing 0.23 M p-benzoquinone. The electrodeposition process was carried out using a three-electrode system at -0.1 V versus Ag/AgCl for 5 minutes. Following electrodeposition, 0.2 mL of dimethyl sulfoxide (DMSO) solution containing 0.2 M vanadyl acetylacetonate

($VO(acac)_2$) was dropped on the BiOI electrodes. The resulting electrodes was heated in a muffle furnace at 450 °C (2 hours), with a ramp rate of 2 °C min^{-1}. To eliminate excess V_2O_5, the photoanodes underwent a 30 min immersion in a 1 M K_3BO_3 solution. The resulting BV photoanodes, were then washed with deionized water and dried in ambient air.

Preparation of BV/FeNi(OH)$_X$ photoanodes： BV/FeNi(OH)$_X$ electrodes were fabricated via electrodeposition technique. In a typical procedure, the cathodic deposition process was conducted by a three-electrode system at -0.7 V versus Ag/AgCl (60 seconds) under room temperature conditions. And the electrolyte containing 8 mM $FeSO_4·7H_2O$ and 8 mM $Ni(NO_3)_2·6H_2O$ was obtained in deionized water.

Preparation of BV/Fe(OH)$_X$-L photoanodes： The BV/Fe(OH)$_X$-L photoanodes were synthesized by the same procedure. Typically, an electrolyte containing 16 mM $FeSO_4·7H_2O$ was achieved in deionized water. The cathodic deposition process for this synthesis occurred at room temperature, maintaining a constant potential of -0.3 V versus Ag/AgCl for a duration of 70 seconds. Subsequently, the final product was obtained and denoted as BV/Fe(OH)$_X$-L.

Preparation of BV/Fe(OH)$_X$-H photoanodes： The Fe(OH)$_X$-H was coated onto the surface of BV by the same procedure. Specially, the solution containing of 16 mM $FeSO_4·7H_2O$ was prepared by using deionized water and subjected to heating at 70 ℃.

Preparation of BV/Fe(OH)$_X$-L/FeNi(OH)$_X$ photoanodes： The preparation of BV/Fe(OH)$_X$-L/FeNi(OH)$_X$ photoanodes involved a two-step process. Initially, BV/Fe(OH)$_X$-L photoanodes were obtained following the aforementioned procedure. Subsequently, electrodeposition was employed to gain BV/Fe(OH)$_X$-L/FeNi(OH)$_X$. For this purpose, a solution containing of 8 mM $FeSO_4·7H_2O$ and 8 mM $Ni(NO_3)_2·6H_2O$ was obtained through using deionized water, and the cathodic deposition process for FeNi(OH)$_X$ took place at room temperature, maintaining a constant potential of -0.7 V versus Ag/AgCl for a duration of 60 seconds.

Preparation of BV/Fe(OH)$_X$-H/FeNi(OH)$_X$ photoanodes： The FeNi(OH)$_X$ was coated onto the surface of BV/Fe(OH)$_X$-H photoanodes by the same procedure.

Preparation of BV/CoFe(OH)$_X$ and BV/Fe(OH)$_X$-H/CoFe(OH)$_X$ photoanodes： BV/CoFe(OH)$_X$ electrodes were fabricated *via* electrodeposition technique. Firstly, an electrolytic solution consisting of 8 mM $FeSO_4·7H_2O$ and 8 mM $Co(NO_3)_2·6H_2O$ was achieved via using deionized water. Subsequently, the cathodic deposition process was

conducted by a three-electrode system at -0.7 V versus Ag/AgCl (60 seconds) under room temperature condition. The preparation of BV/$Fe(OH)_X$-H/$CoFe(OH)_X$ photoanodes also involved a two-step procedure. Importantly, BV/$Fe(OH)_X$-H photoanodes were prepared at 70 °C using the same methodology as described previously.

S 3. Additional Figures and Discussions

S 3.1 Experimental Data

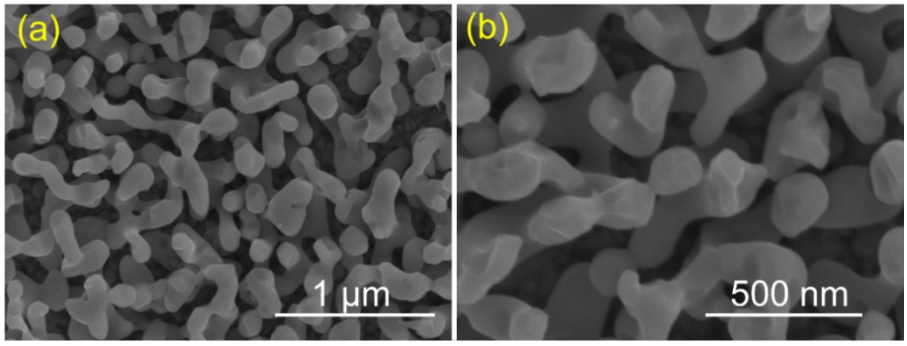

Fig. S1 SEM images of the $BiVO_4$ (BV).

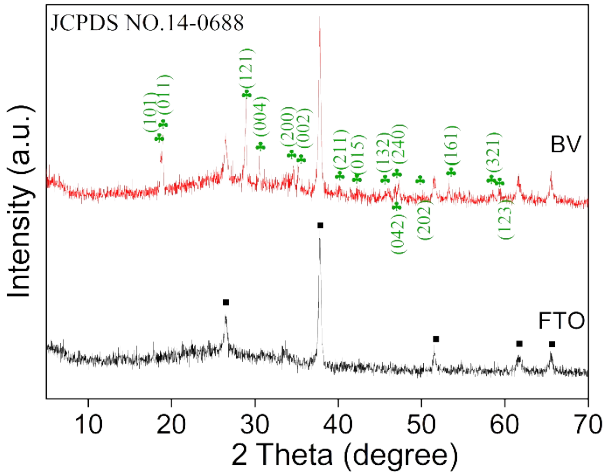

Fig. S2 XRD patterns of FTO and BV.

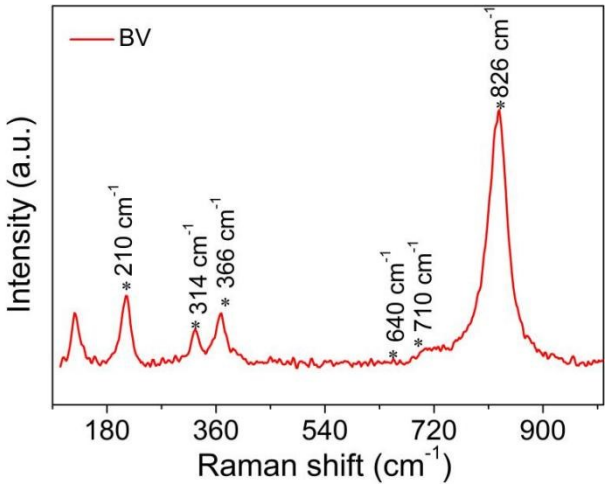

Fig. S3 Raman spectra of BV.

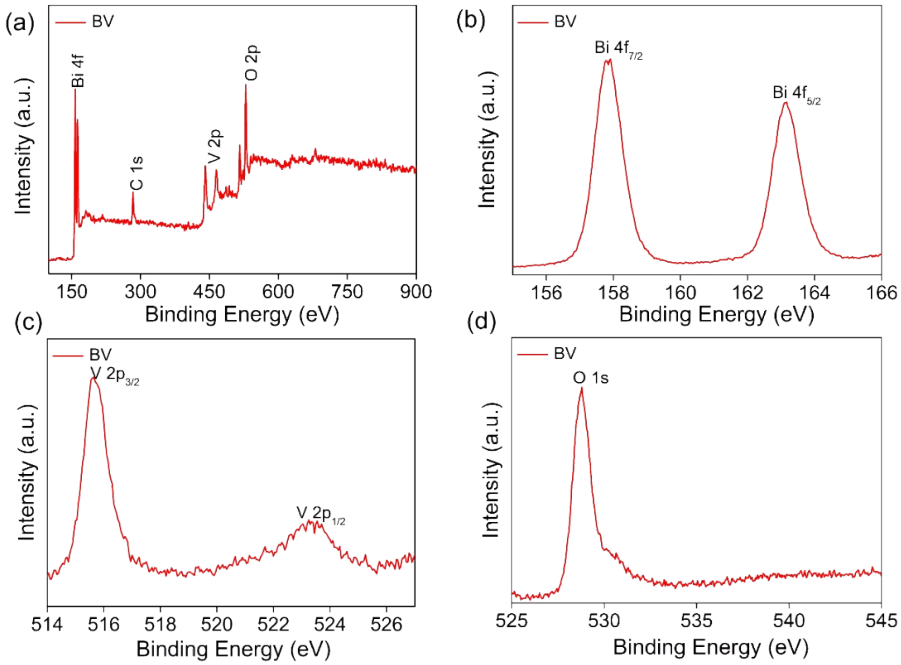

Fig. S4 XPS survey spectra and high-resolution XPS spectra of BV.

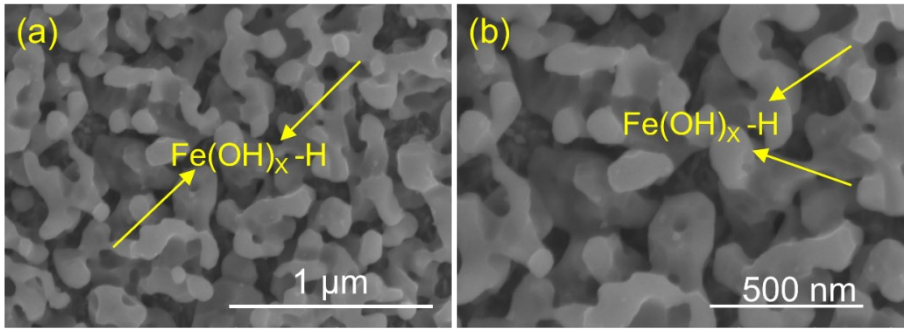

Fig. S5 SEM images of the BV/$Fe(OH)_X$-H (where H stands for the nature of highly crystalline $Fe(OH)_X$).

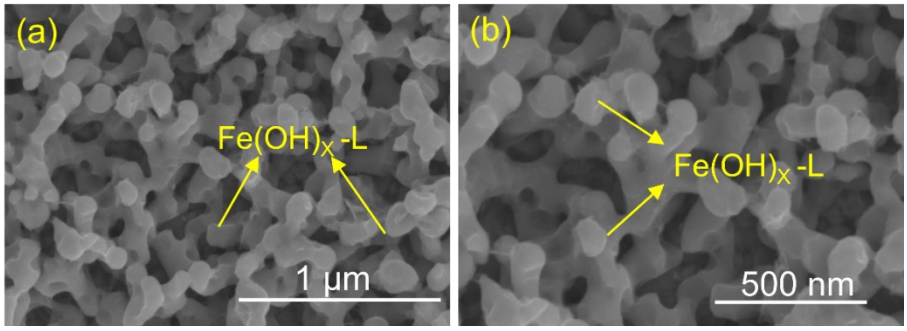

Fig. S6 SEM images of the BV/$Fe(OH)_X$-L (where L stands for the nature of low crystalline $Fe(OH)_X$).

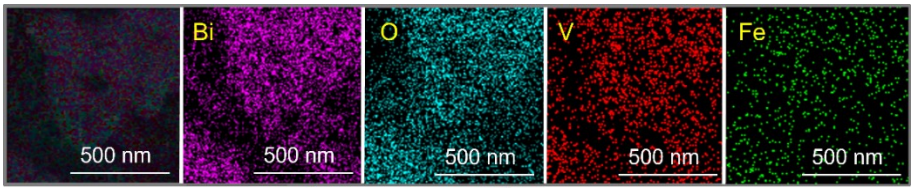

Fig. S7 The elemental mapping images of the BV/Fe(OH)$_X$-H.

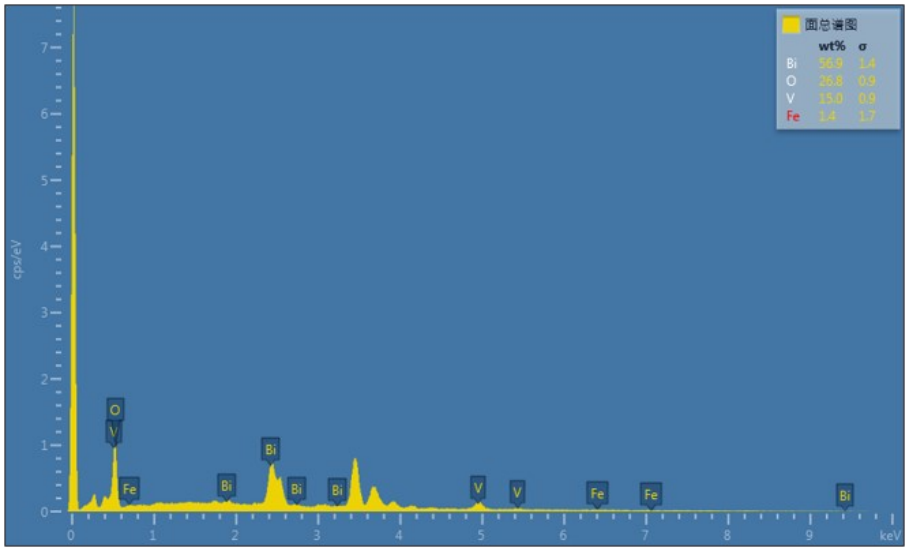

Fig. S8 SEM-EDS of the BV/Fe(OH)$_X$-H.

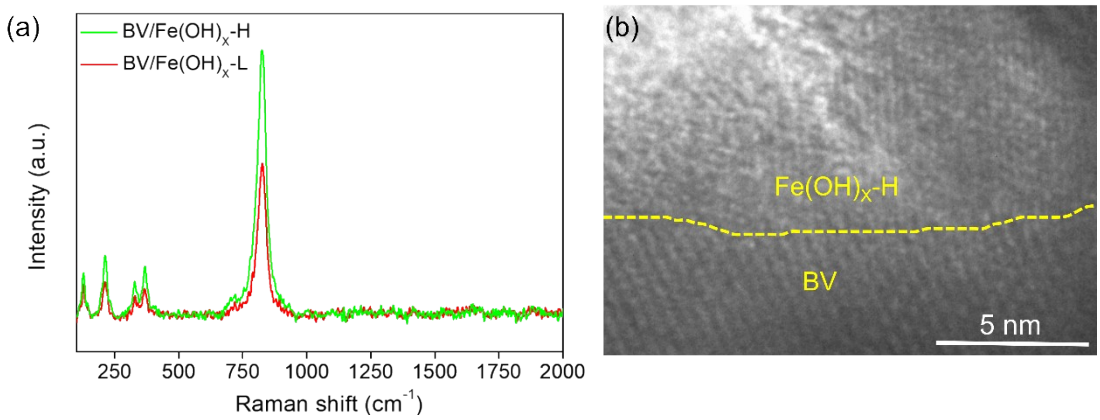

Fig. S9 (a) Raman spectra of BV/$Fe(OH)_X$-H and BV/$Fe(OH)_X$-L. (b) HRTEM of BV/$Fe(OH)_X$-H.

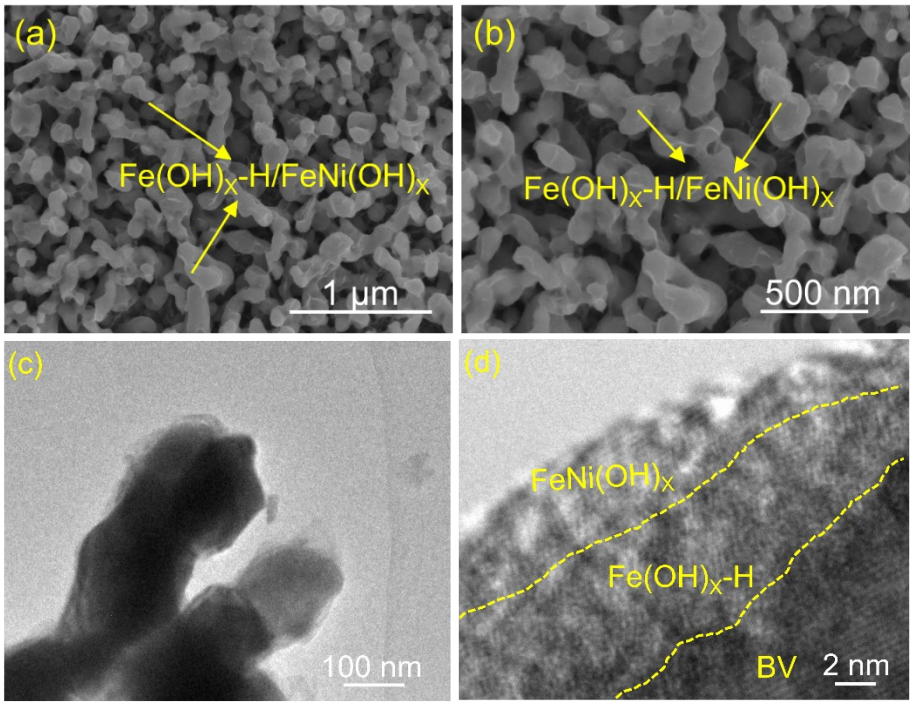

Fig. S10 (a and b) SEM images of the BV/$Fe(OH)_X$-H/$FeNi(OH)_X$. (c) TEM of BV/$Fe(OH)_X$-H/$FeNi(OH)_X$. (d) HRTEM of BV/$Fe(OH)_X$-H/$FeNi(OH)_X$.

HR-TEM was employed to observe the structure of BV/$Fe(OH)_X$-H/$FeNi(OH)_X$. As shown in Fig. S10, the consecutive layers, including $Fe(OH)_X$-H and $FeNi(OH)_X$, can be detected for BV/$Fe(OH)_X$-H/$FeNi(OH)_X$, further confirming the presence of $Fe(OH)_X$-H and $FeNi(OH)_X$ on the surface of BV.

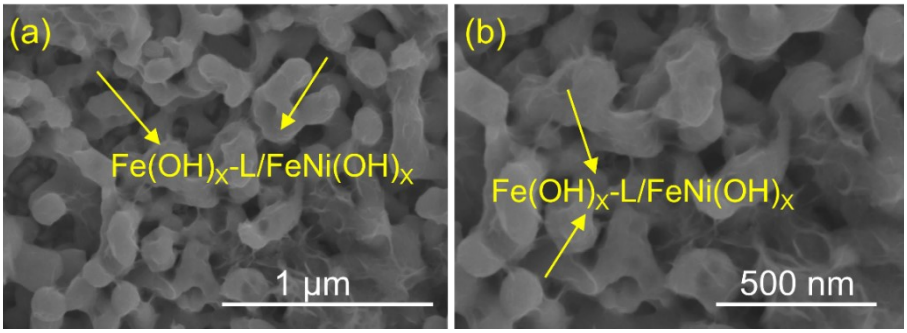

Fig. S11 SEM images of the BV/$Fe(OH)_X$-L/$FeNi(OH)_X$.

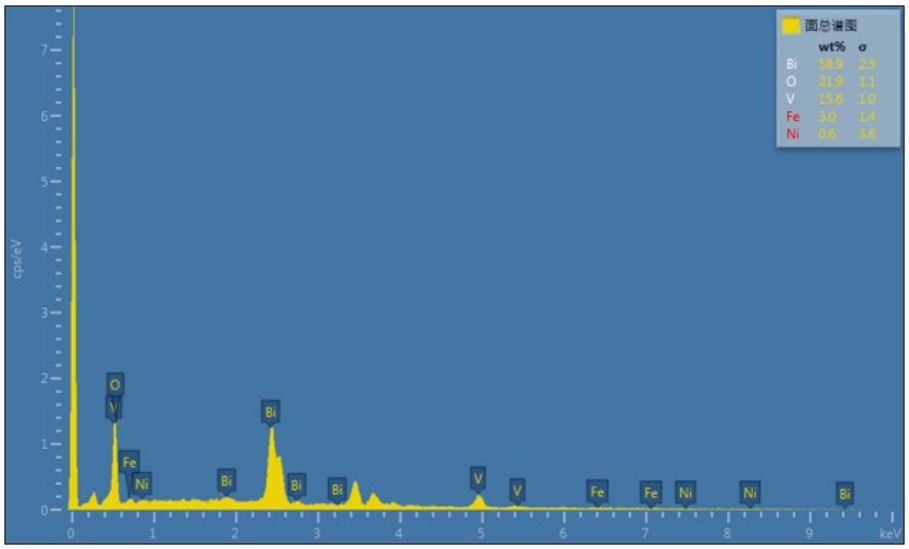

Fig. S12 SEM-EDS of the BV/$Fe(OH)_X$-H/$FeNi(OH)_X$.

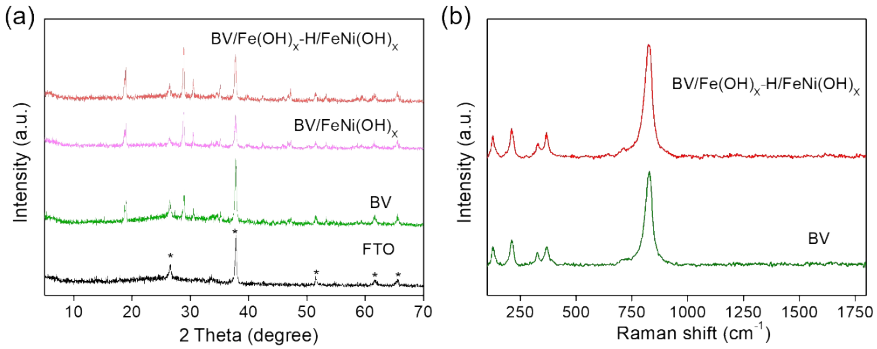

Fig. S13 (a) XRD patterns and BV, BV/FeNi(OH)$_X$, and BV/Fe(OH)$_X$-H/FeNi(OH)$_X$. (b) Raman spectra of BV and BV/Fe(OH)$_X$-H/FeNi(OH)$_X$.

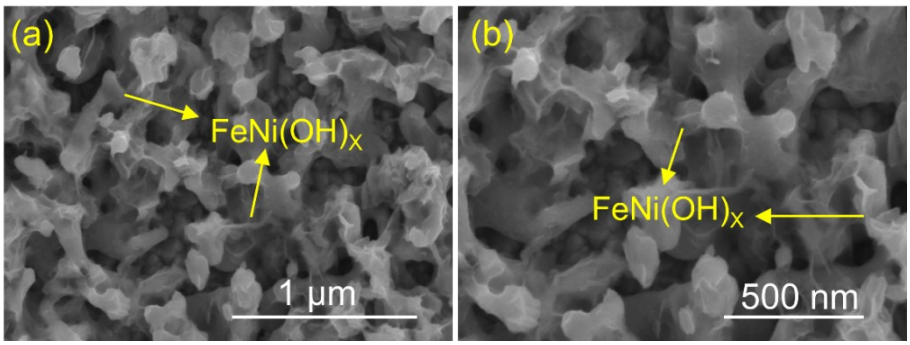

Fig. S14 SEM images of the BV/FeNi(OH)$_X$.

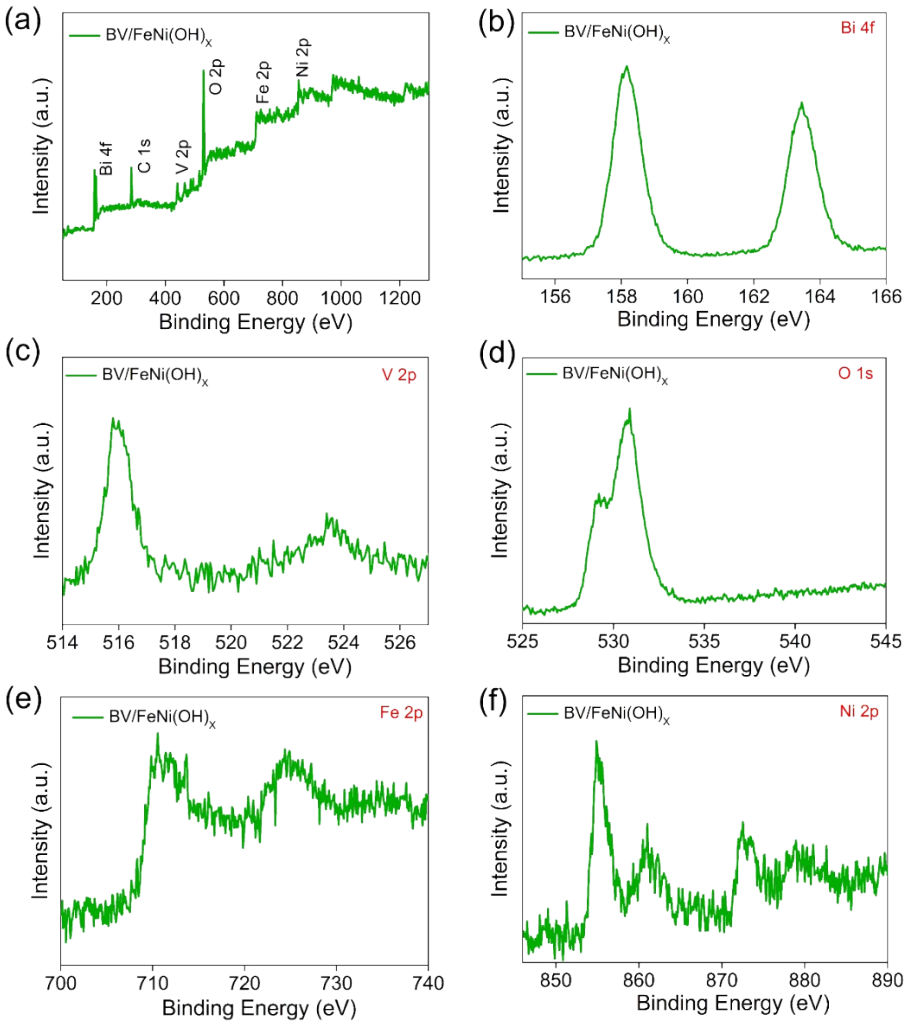

Fig. S15 XPS spectra of BV/FeNi(OH)$_X$.

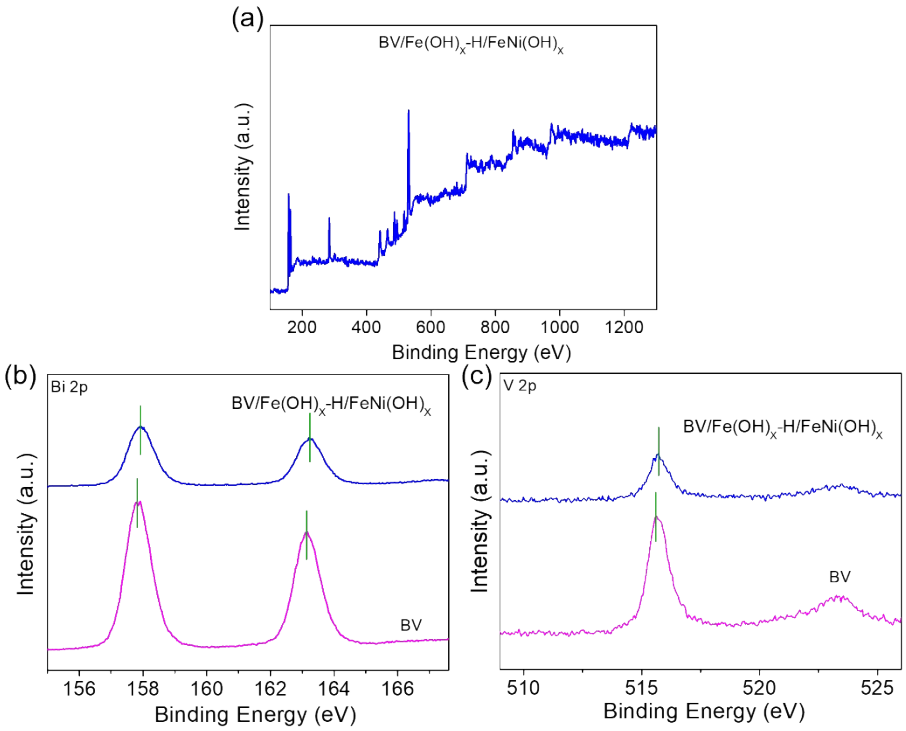

Fig.S16 (a) XPS survey spectra of $BV/Fe(OH)_X$-H/$FeNi(OH)_X$. (b) Bi 4f and (c) V 2p spectra of different photoanodes.

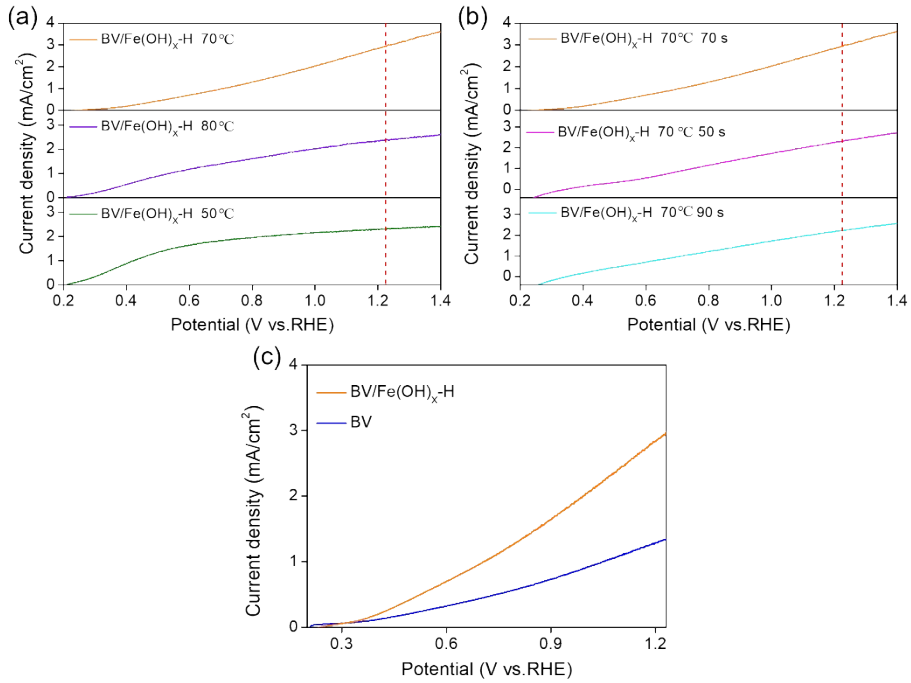

Fig. S17 *J-V* curves of different photoanodes under AM 1.5 G (100 mW/cm^2) illumination.

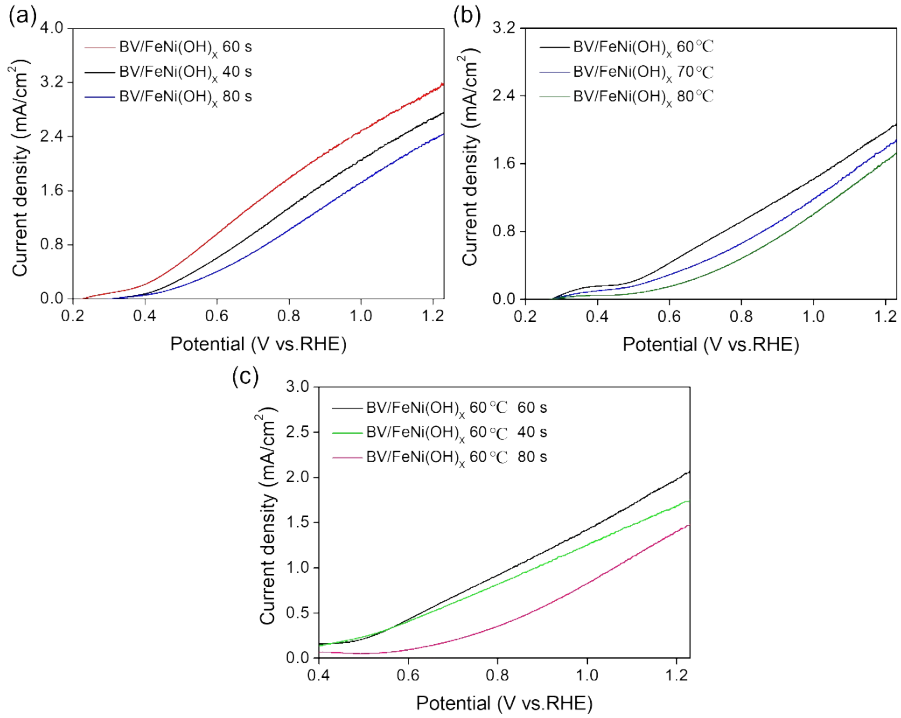

Fig. S18 Photocurrent densities of BV/FeNi(OH)$_X$ with different deposition time and temperature.

As presented in Fig. S18, compared with the optimized BV/FeNi(OH)$_X$, the as prepared BV/FeNi(OH)$_X$ photoanode (at the room temperature, Fig. S18a) still exhibits a high photocurrent density, because amorphous FeNi(OH)$_X$ offers more active catalytic sites for the accelerated water oxidation kinetics.

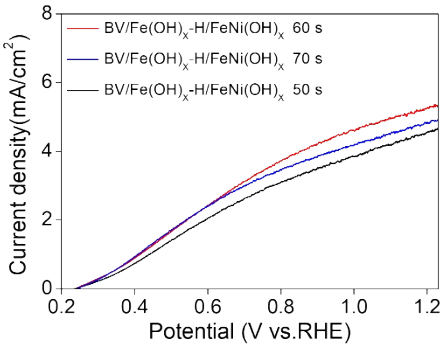

Fig. S19 Photocurrent densities of BV/Fe(OH)$_X$-H/FeNi(OH)$_X$ with different time.

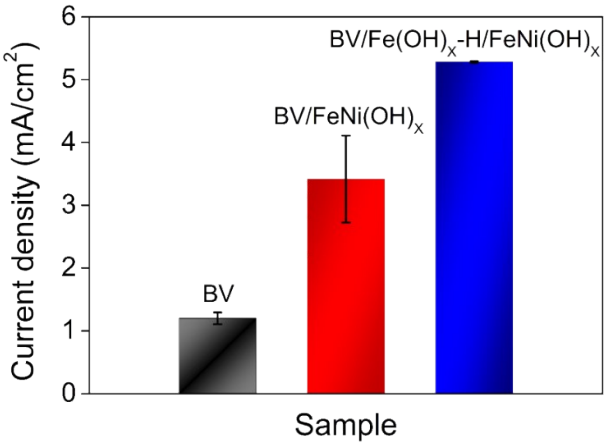

Fig. S20 Photocurrent densities of different samples.

Fig. S20 exhibits the repeatability of different samples, and BV/Fe(OH)$_X$-H/FeNi(OH)$_X$ shows an outstanding stability.

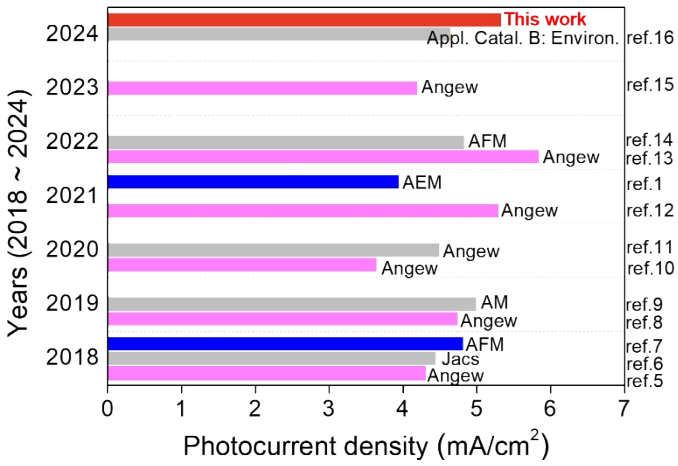

Fig. S21 Photocurrent densities based on BV-based photoanodes at the 1.23 V_{RHE} in recent years (2018 ~ 2024).

Based on Fig. S21 and Table S1, the BV/Fe(OH)$_X$-H/FeNi(OH)$_X$ photoanode shows a higher photocurrent density compared to other BV-based photoelectrodes.

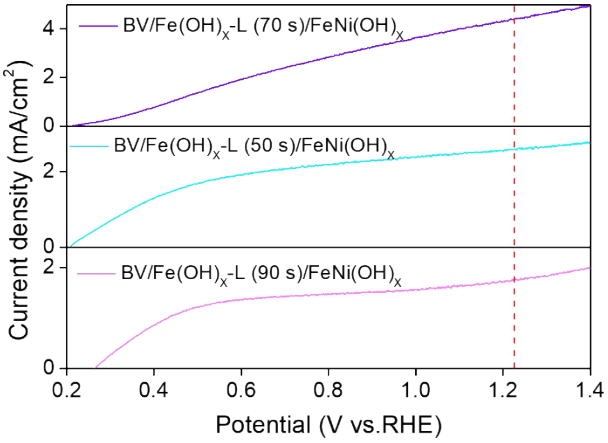

Fig. S22 Photocurrent densities of different samples.

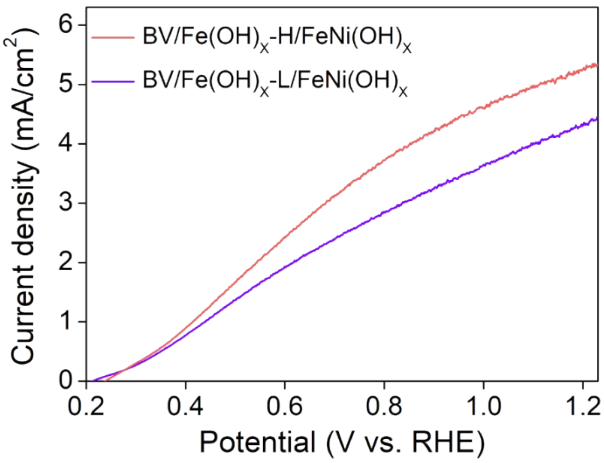

Fig. S23 Photocurrent densities of different samples.

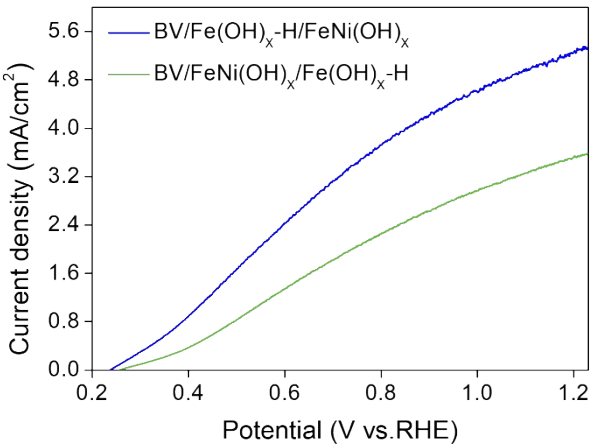

Fig. S24 Photocurrent density of BV/FeNi(OH)$_X$/Fe(OH)$_X$-H.

As presented in Fig. S24, the BV/FeNi(OH)$_X$/Fe(OH)$_X$-H photoanode still exhibits a lower photocurrent density compared to BV/Fe(OH)$_X$-H/FeNi(OH)$_X$. Therefore, we can conclude that the impressive enhancement in PEC performance is due to the Fe(OH)$_X$-H, which can quickly transfer hole to FeNi(OH)$_X$ surface for subsequent water oxidation.

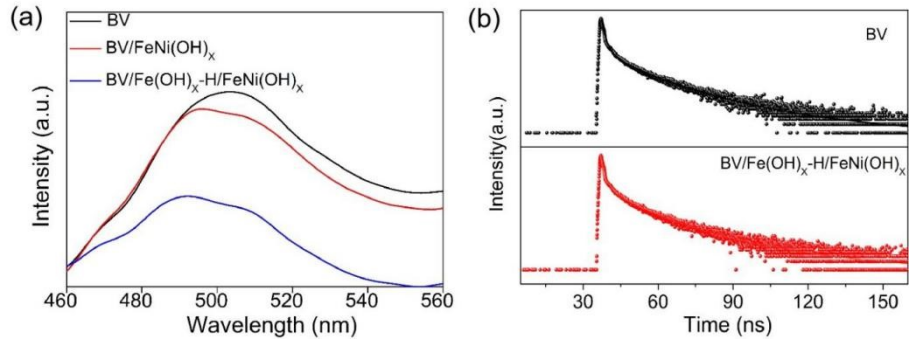

Fig. S25 (a) PL spectra of different photoanodes with excitation of 350 nm. (b) TRPL spectra of different photoanodes.

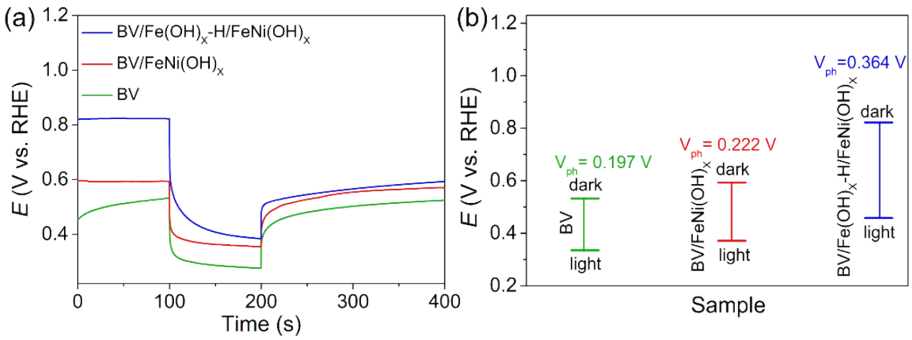

Fig. S26 (a) The open circuit potential (OCP) versus time curves measured in a 0.5 M PBS. (b) Normalized OCP decay profiles for different samples.

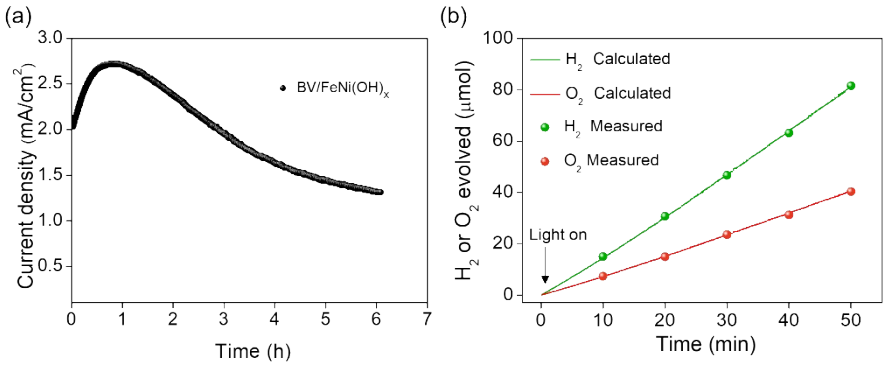

Fig. S27 (a) *I-t* stability test for BV/FeNi(OH)$_X$ (b)Hydrogen (H_2) and oxygen (O_2) evolution of the BV/Fe(OH)$_X$-H/FeNi(OH)$_X$ photoanode.

At the initial 1 h, an increased tendency in photocurrent density may contribute to the transformation of FeNi(OH)$_X$ (Fig. S27a), where high valence ions mainly act as the active site for water oxidation reaction. The amounts of H_2 and O_2 from BV/Fe(OH)$_X$-H/FeNi(OH)$_X$ were measured by gas chromatography (Fig. S27b).

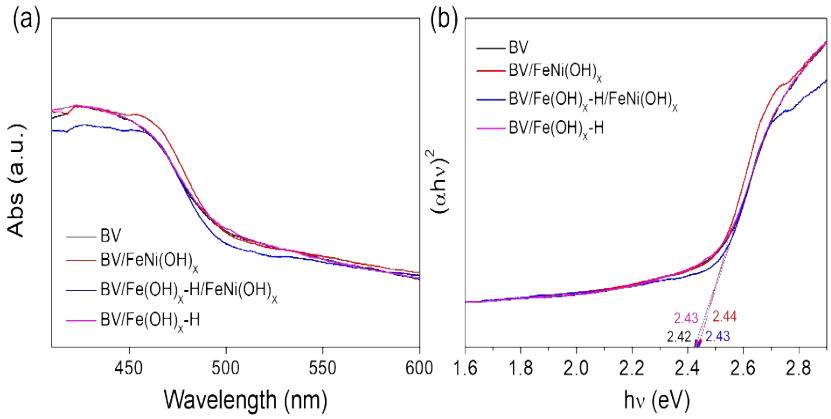

Fig. S28 DRS and Tauc plots of different samples.

The solid-state UV-vis spectra (DRS) results of corresponding samples show very similar absorption range (Fig. S28a), and the band gap values of $BV/Fe(OH)_X$-$H/FeNi(OH)_X$, $BV/FeNi(OH)_X$, $BV/Fe(OH)_X$-H, BV are 2.43 eV, 2.44 eV, 2.43eV and 2.42 eV (Fig. S28b), respectively, through Kubelka-Munk transformation.

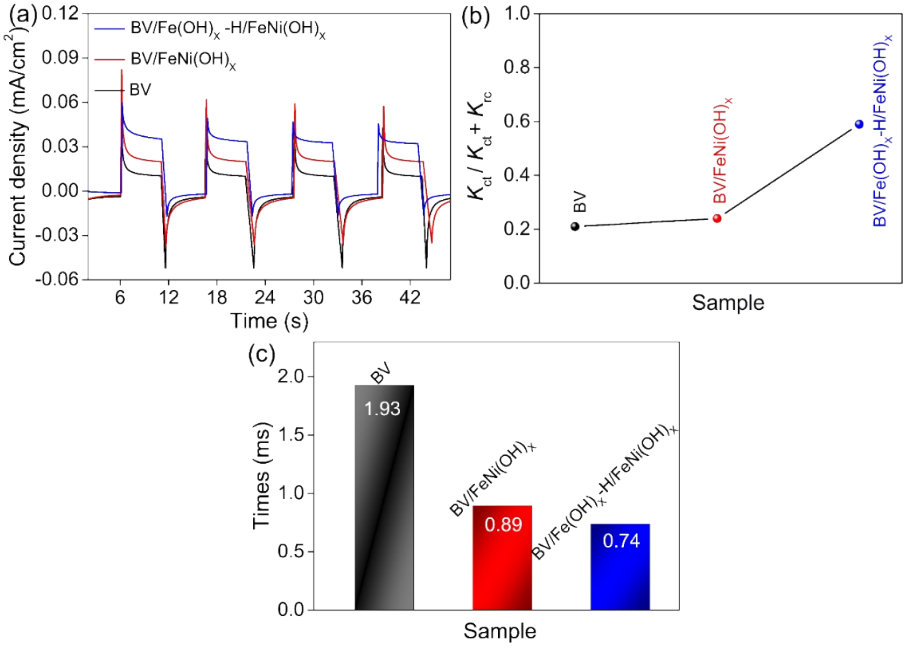

Fig. S29 (a) *I-t* curves of different photoanodes. (b) Charge transfer efficiency results. (c) Transit time of different samples.

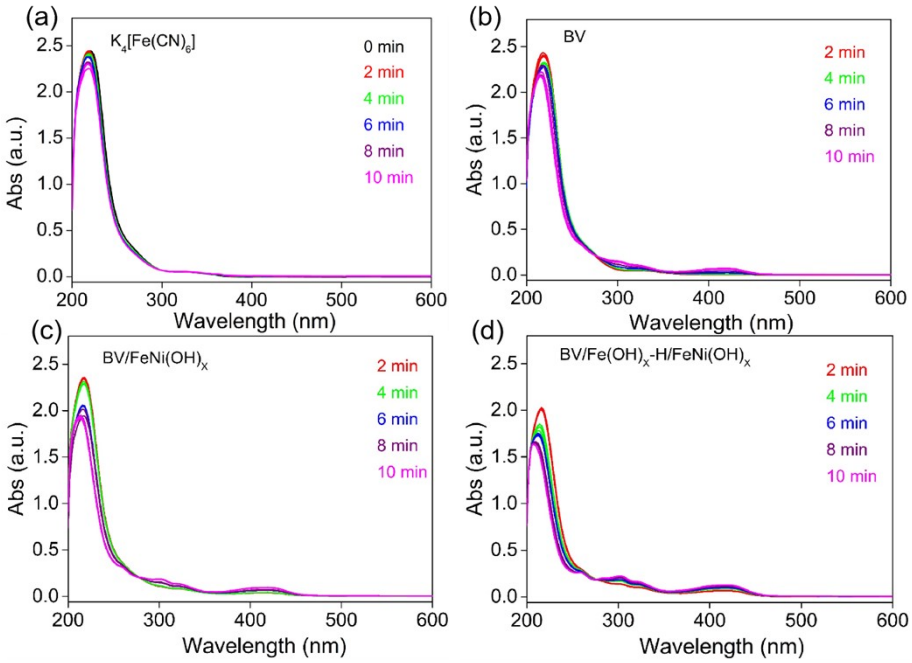

Fig. S30 Time-dependent absorption spectra of $K_4[Fe(CN)_6]$ under light condition.

Herein, *in situ* UV/vis-SEC platform was carried out to investigate the absorption of $K_4[Fe(CN)_6]$ (Fig. S30). More importantly, the absorbance of different systems is different during reactions, meaning the photogenerated holes can easily transfer from the BV directly to the $FeNi(OH)_X$ surface through the “hole porter”.

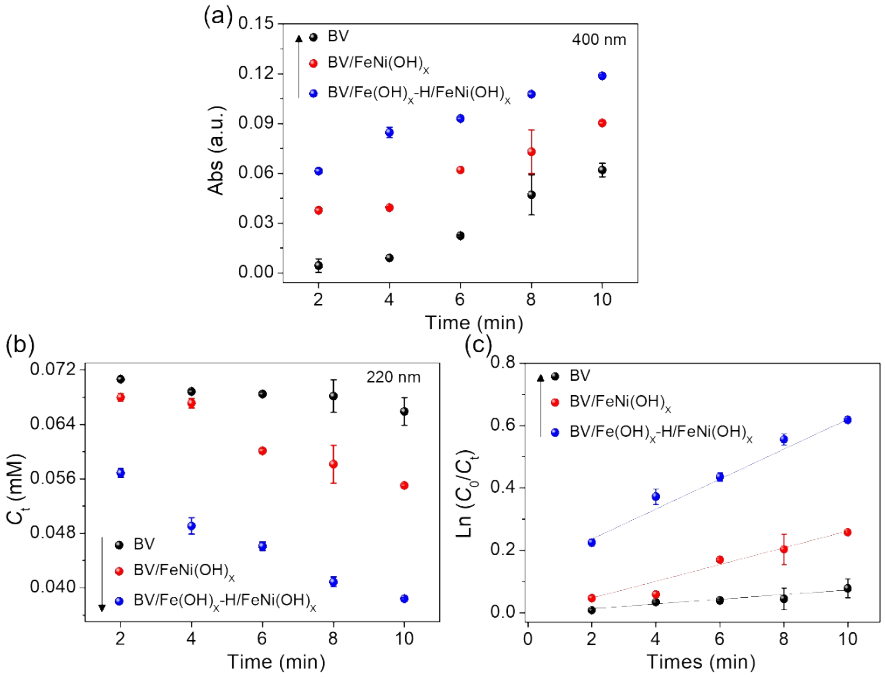

Fig. S31 (a) Results of time-dependent concentration of $K_3[Fe(CN)_6]$. (b) Results of time-dependent concentration of of $K_4[Fe(CN)_6]$. (c) Results of time-dependent concentration of $K_4[Fe(CN)_6]$ during oxidation process.

In Fig. S31a, the absorbance of $K_3[Fe(CN)_6]$ in BV/$Fe(OH)_X$-H/$FeNi(OH)_X$ system shows significantly increased compared to other samples, suggesting that hole is easily migrated to the photoanodes' surface to participate in oxidation reaction of $K_4[Fe(CN)_6]$. On the contrary, on a certain time scale (Fig. S31b), the concentration of $K_4[Fe(CN)_6]$ shows a decreasing trend. Based on the above analysis, we can obtain the correspondingly hole transfer kinetics i.e., K_{ab} by first-order kinetic model (Fig. S31c).

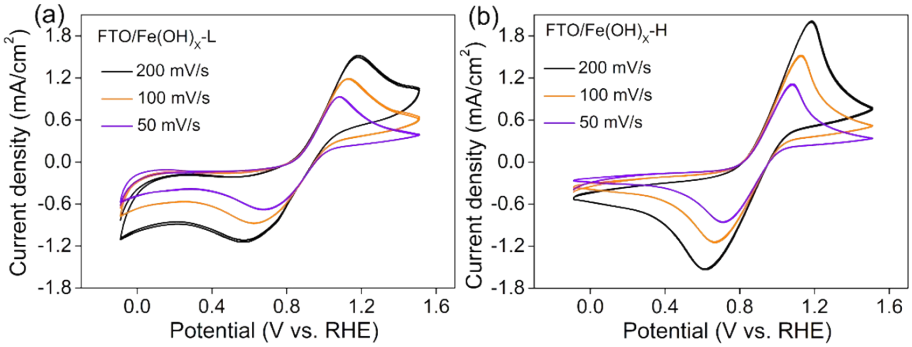

Fig. S32 CV curves of different samples with different scan rates.

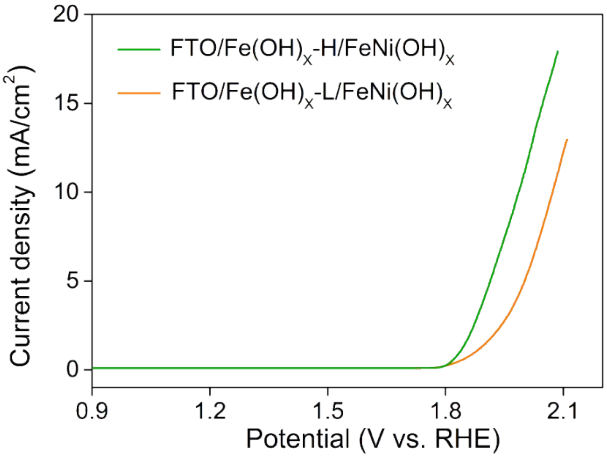

Fig. S33 *iR*-corrected LSV curves of different samples on FTO.

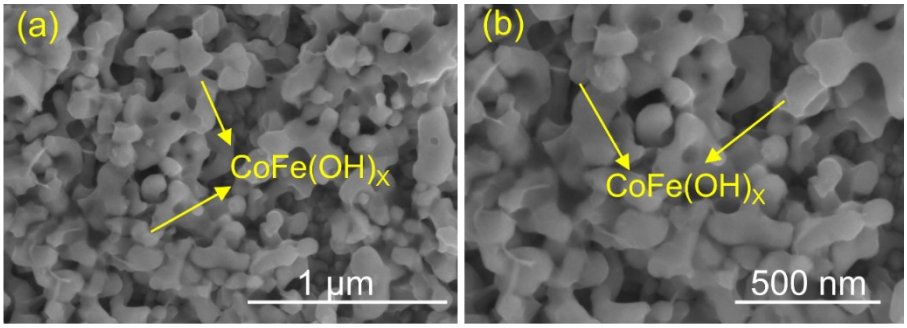

Fig. S34 SEM images of BV/$CoFe(OH)_X$.

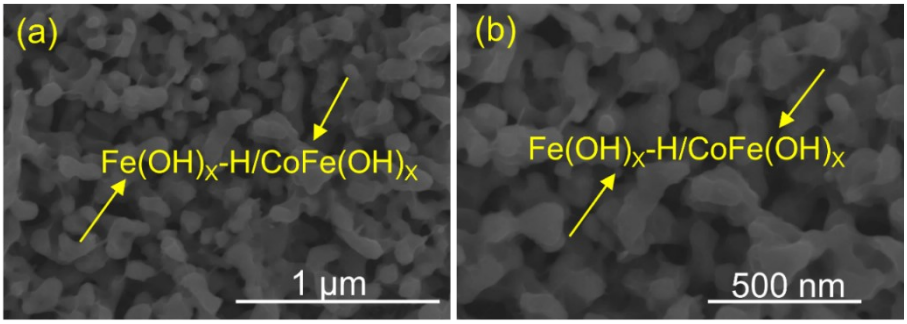

Fig. S35 SEM images of BV/$Fe(OH)_X$-H/$CoFe(OH)_X$.

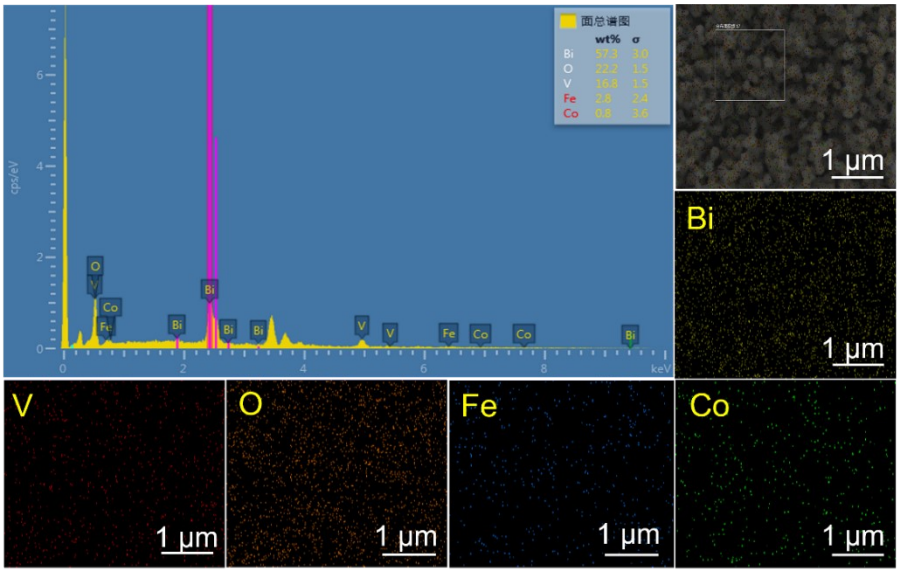

Fig. S36 SEM-EDS of BV/$Fe(OH)_X$-H/$CoFe(OH)_X$.

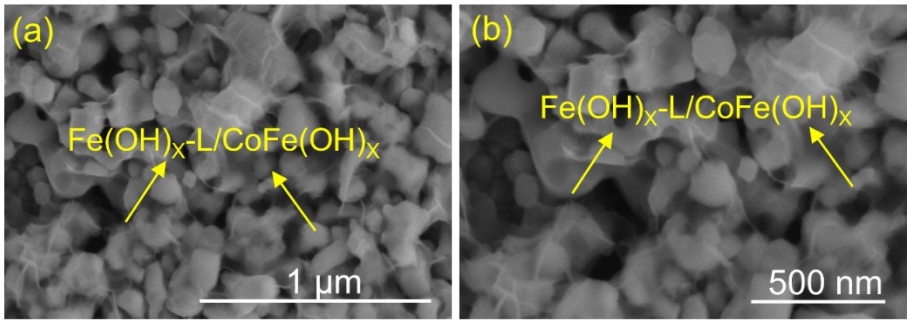

Fig. S37 SEM images of BV/$Fe(OH)_X$-L/$CoFe(OH)_X$.

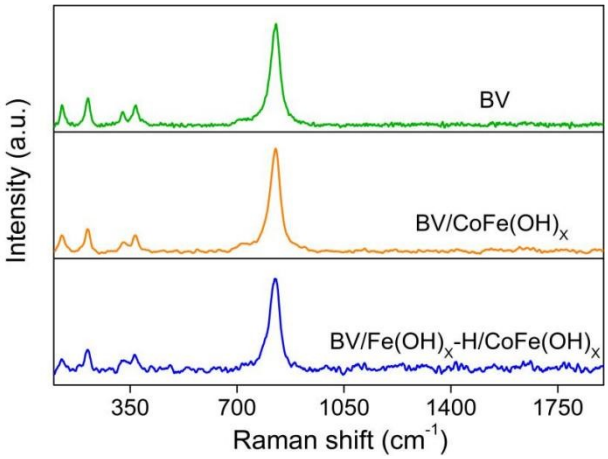

Fig. S38 Raman spectra of BV, BV/CoFe(OH)$_X$, and BV/Fe(OH)$_X$-H/CoFe(OH)$_X$.

Table S1. Summary of recent significant progress of BV-based photoanodes.

Photoanodes	Photocurrent at 1.23 V vs. RHE	Journal	Year	Ref
BV/β-FeOOH	4.30 mA/cm^2	*Angew. Chem. Int. Ed.*	2018	5
BV/LDH/pGO/$CoPO_3$	4.45 mA/cm^2	*J. Am. Chem. Soc.*	2018	6
BV/$FeCoO_X$	4.82 mA/cm^2	*Adv. Funct. Mater.*	2018	7
BV-VO/Co-Pi	5.00 mA/cm^2	*Adv. Mater.*	2019	8
R-BV/CoPy/FN-H	4.75 mA/cm^2	*Angew. Chem. Int. Ed.*	2019	9
BV/PE	4.50 mA/cm^2	*Angew. Chem. Int. Ed.*	2020	10
BV/F_1N_3-H	3.65 mA/cm^2	*Angew. Chem. Int. Ed.*	2020	11
Ov-BV/NiFe-MOFs	5.30 mA/cm^2	*Angew. Chem. Int. Ed.*	2021	12
BV/$Co(OH)_X$-Ag	3.95 mA/cm^2	*Adv. Energy Mater.*	2021	1
BV/MQD/MoO_X/NiFeOOH	5.85 mA/cm^2	*Angew. Chem. Int. Ed.*	2022	13
C-BV/CQDs	4.83 mA/cm^2	*Adv. Funct. Mater.*	2022	14
$BV_{6\%}$/$NiFeO_X$	4.20 mA/cm^2	*Angew. Chem. Int. Ed.*	2023	15
$BiVO_4$@NiFe-LDHs/Ru	4.65 mA/cm^2	*Appl. Catal., B Environ.*	2024	16
BV/$Fe(OH)_X$-H/$FeNi(OH)_X$	**5.34 mA/cm^2**	**Present work**		

Table S2. EIS of different samples under light condition.

Samples	BV	BV/$FeNi(OH)_X$	BV/$Fe(OH)_x$-H/$FeNi(OH)_X$
R_s / (Ω)	42.8	41.1	41.6
R_{ct} / (Ω)	3970	986	603

Table S3. The average fluorescence lifetime of BV/$Fe(OH)_X$-H/$FeNi(OH)_X$ and BV.

Samples	τ_1 / (ns)	τ_2 / (ns)	τ / (ns)
BV	3.03	13.60	3.46
BV/$Fe(OH)_x$-H/$FeNi(OH)_x$	3.14	13.80	4.03

Table S4. Transit time values of different samples.

Samples	BV	BV/$FeNi(OH)_X$	BV/$Fe(OH)_x$-H/$FeNi(OH)_X$
f_{Imps} / (Hz)	82.54	177.83	215.44
τ_d / (ms)	1.93	0.89	0.74

Table S5. EIS of different samples under dark condition.

Samples	BV	BV/$FeNi(OH)_X$	BV/$Fe(OH)_X$-H/$FeNi(OH)_X$
R_s / (Ω)	40.5	41.4	42.6
R_{ct} / (kΩ)	91.2	50.9	14.1

Table S6. EIS of different samples under light condition.

Samples	BV	BV/$CoFe(OH)_X$	BV/$Fe(OH)_X$-H/$CoFe(OH)_X$
R_s / (Ω)	42.8	47	43.8
R_{ct} / (Ω)	3970	1030	705

S 3.2 Reference

1. X. Ning, D. Yin, Y. Fan, Q. Zhang, P. Du, D. Zhang, J. Chen and X. Lu, *Adv. Energy Mater*, 2021, **11**, 2100405.

2. B. Liu, X. Wang, Y. Zhang, L. Xu, T. Wang, X. Xiao, S. Wang, L. Wang and W. Huang, *Angew. Chem. Int. Ed*., 2023, **62**, 202217346.

3. H. Choi, Y. Y. Kim, S. Seo, Y. Jung, S.-M. Yoo, C. S. Moon, N. J. Jeon, S. Lee, K. Lee, F. M. Toma, J. Seo and S. Lee, *Adv. Energy Mater*. 2023, **13**, 2300951.

4. H.-J. Ahn, K.-Y. Yoon, M. Sung, H. Yoo, H. Ahn, B. H. Lee, J. Lee and J. Jang, *ACS Energy Lett*. 2023, **8**, 2595.

5. B. Zhang, L. Wang, Y. Zhang, Y. Ding and Y. Bi, *Angew. Chem. Int. Ed*., 2018, **57**, 2248.

6. S. Ye, C. Ding, R. Chen, F. Fan, P. Fu, H. Yin, X. Wang, Z. Wang, P. Du and C. Li, *J. Am. Chem. Soc*. 2018, **140**, 3250.

7. S. Wang, T. He, J. H. Yun, Y. Hu, M. Xiao, A. Du and L. Wang, *Adv. Funct. Mater*. 2018, **28**, 1802685.

8. H. Ren, T. Dittrich, H. Ma, J. N. Hart, S. Fengler, S. Chen, Y. Li, Y. Wang, F. Cao and M. Schieda, *Adv. Mater*. 2019, **31**, 1807204.

9. X. Ning, B. Lu, Z. Zhang, P. Du, H. Ren, D. Shan, J. Chen, Y. Gao and X. Lu, *Angew. Chem. Int. Ed*., 2019, **58**, 16800.

10. S. Feng, T. Wang, B. Liu, C. Hu, L. Li, Z. J. Zhao and J. Gong, *Angew. Chem. Int. Ed*., 2020, **132**, 2060.

11. X. Ning, P. Du, Z. Han, J. Chen and X. Lu, *Angew. Chem. Int. Ed*., 2021, **60**, 3504.

12. J. B. Pan, B. H. Wang, J. B. Wang, H. Z. Ding, W. Zhou, X. Liu, J. R. Zhang, S. Shen, J. K. Guo and L. Chen, *Angew. Chem. Int. Ed*., 2021, **60**, 1433.

13. Y. Song, X. Zhang, Y. Zhang, P. Zhai, Z. Li, D. Jin, J. Cao, C. Wang, B. Zhang, J. Gao, L. Sun and J. Hou, *Angew. Chem. Int. Ed*., 2022, **134**, 202200946.

14. Y. Wang, D. Chen, J. Zhang, M. S. Balogun, P. Wang, Y. Tong and Y. Huang, *Adv. Funct. Mater*. 2022, **32**, 2112738.

15. N. Yang, S. Zhang, Y. Xiao, Y. Qi, Y. Bao, P. Xu, S. Jin and F. Zhang, *Angew. Chem. Int. Ed*., 2023, **62**, 202308729.

16. Y. Sun, H. Li, Y. Hu, J. Wang, A. Li and P. *Appl. Catal., B Environ.* 2024, **340**, 123269.